

From Relative Azimuth to Absolute Location: Pushing the Limit of PIR Sensor based Localization

Xuefeng Liu*

State Key Lab. of VR Tech. & Sys.
School of C.S.E., BeiHang University
liu_xuefeng@buaa.edu.cn

Tianye Yang*

School of Electronic and Infor. Engi.,
Huazhong Univ. of Sci. and Tech.
d201677515@hust.edu.cn

Shaojie Tang

Naveen Jindal School of Management,
University of Texas at Dallas
shaojie.tang@utdallas.edu

Peng Guo

School of Electronic and Information
Engineering, Huazhong University of
Science and Technology
guopeng@hust.edu.cn

Jianwei Niu

State Key Lab. of VR Tech. & Sys.
School of C.S.E., BeiHang University
Beijing Adv. Innov. CTR for BDBC
niujianwei@buaa.edu.cn

ABSTRACT

Pyroelectric infrared (PIR) sensors are considered to be promising devices for device-free localization due to its advantages of low cost, energy efficiency, and the immunity from multi-path fading. However, most of the existing PIR-based localization systems only utilize the binary information of PIR sensors and therefore require a large number of carefully deployed PIR sensors. A few works directly map the raw data of PIR sensors to one's location using machine learning approaches. However, these data-driven approaches require abundant training data and suffer from environmental change. In this paper, we propose PIRATES, a PIR-based device-free localization system based on the raw data of PIR sensors. The key of PIRATES is to extract a new type of location information called azimuth change. The extraction of the azimuth change relies on the physical properties of PIR sensors. Therefore, no abundant training data are needed and the system is robust to environmental change. Through experiments, we demonstrate that PIRATES can achieve higher localization accuracy than the state-of-the-art approaches. In addition, the information of the azimuth change can be easily incorporated with other information of PIR signals (e.g. amplitude) to improve the localization accuracy.

CCS CONCEPTS

- Human-centered computing → Ubiquitous and mobile computing.

KEYWORDS

Device-free Localization; PIR sensors; Inverse filter; Particle filter

*Primary authors with equal contribution.

Permission to make digital or hard copies of all or part of this work for personal or classroom use is granted without fee provided that copies are not made or distributed for profit or commercial advantage and that copies bear this notice and the full citation on the first page. Copyrights for components of this work owned by others than ACM must be honored. Abstracting with credit is permitted. To copy otherwise, or republish, to post on servers or to redistribute to lists, requires prior specific permission and/or a fee. Request permissions from permissions@acm.org.

MobiCom '20, September 21–25, 2020, London, United Kingdom

© 2020 Association for Computing Machinery.

ACM ISBN 978-1-4503-7085-1/20/09...\$15.00

<https://doi.org/10.1145/337224.3380878>

1 INTRODUCTION

Device-free localization has received much attention recently due to the advantage that the target does not need to carry any devices. Various types of device-free localization systems have been developed such as those using cameras [1], light sensors [2], and acoustic sensors [3]. In addition, many RF-based device-free localization systems have been developed, including those using COTS Zigbee nodes [4], RFID devices [5] and WiFi APs [6–8]. Based on the in-depth study of RF communication mechanisms with careful deployment and system designs, the state-of-the-art RF-based localization systems can achieve fairly good localization accuracy, even in a dynamic environment [9, 10].

On the other hand, localization systems based on pyroelectric infrared (PIR) sensors start to attract much interest recently as a promising alternative to existing device-free localization systems [11]. Compared with other types of sensing units like cameras and RF devices, PIR sensors have much lower cost and are more energy efficient. Besides, when compared with the camera-based systems, PIR sensors can work well in low-light environments and have less privacy concerns. When compared with RF-based systems, PIR sensors are immune to multi-path effect [12] and therefore are intrinsically more robust in a changing environment.

Although many PIR-based localization systems have been developed [13–16], most of them rely on the following simple localization strategy. Note that a PIR sensor generates binary information indicating the presence of a person in its detection zone. If we deploy a number of PIR sensors and make their detection zones partially overlap, the person at different locations will trigger different sets of PIR sensors, and they will generate binary vectors like '1010' or '0111'. By continuously collecting the vectors of these PIR sensors, we can obtain one's moving trajectory. The localization accuracy of the above approach is dependent on the granularity of the overlapped zones. The smaller the size, the higher the localization accuracy. As a consequence, it often requires a large number of PIR sensors and a careful deployment to achieve high accuracy.

It should be noted that, the raw value from a PIR sensor is a voltage which reflects the amount of received infrared radiation. The voltage level is then compared with a pre-defined threshold and transforms to a binary value. Transforming an arbitrary voltage value to a binary one generally indicates a large amount of information loss.

Recently, some works start to explore the possibility of directly utilizing the raw voltage instead of binary information of PIR sensors. In [17], a fingerprinting approach is adopted to establish the relationship between one's location and the amplitude of PIR signal, and then implements localization. Similarly, the localization system in [18] first estimates the distance to a person based on the raw data of PIR sensors and then carries out localization. Since raw data contain richer information than the binary one, the number of PIR sensors required by a localization system is greatly reduced. However, the performance of the above systems depends heavily on both the quantity and quality of their training data, which may not be available in a new environment.

In this paper, we develop a novel PIR-based localization system named PIRATES. PIRATES improves the localization accuracy by utilizing a new type of information, called **azimuth change**. The azimuth change is defined as the absolute difference of the azimuth of a person w.r.t a PIR sensor at two locations. For example, as shown in Fig. 1, when a person moves from A to B, the corresponding azimuth change w.r.t the 4 PIR sensors are $\theta_1 - \theta_3$, $\theta_2 - \theta_4$, respectively.

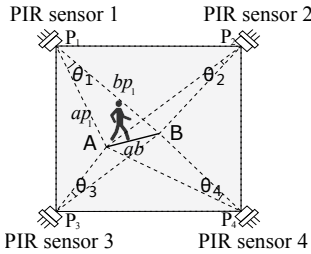


Figure 1: An example of the azimuth change.

We find that the azimuth change contains important information that can be used alone to achieve a high localization accuracy. In addition, unlike the data-driven method proposed in [17] and [18], the azimuth change can be extracted from the raw data of a PIR sensor based on its physical model and therefore does not heavily rely on the labeled training data.

The key problem then becomes how to extract the azimuth change from the raw data of PIR sensors. Our approach is motivated by the following observations. A PIR sensor is often covered by a Fresnel lens array [19], which virtually divides the sensing zone of the PIR sensor into many evenly spaced fan-shaped zones, as shown in the left of Fig. 2. Therefore, to know the azimuth change of the person when he moves from A to B, we need know (1) the number of fan-shaped zones covered by the trace A-B, and (2) the azimuth change corresponding to two neighboring fan-shaped zones. With regard to identifying the first parameter, we show that when a person moves from A to B, the output of a PIR sensor oscillates like a sine wave, as shown in Fig. 2. And the number of rising and falling edges of the sine wave equals to the number of the fan-shaped zones crossed. The second parameter can be calculated based on the geometric parameters of PIR sensors. The estimation of these two parameters will be described in Section 3.

Although the basic idea of estimating the azimuth change is not complicated, its implementation entails several challenges. For

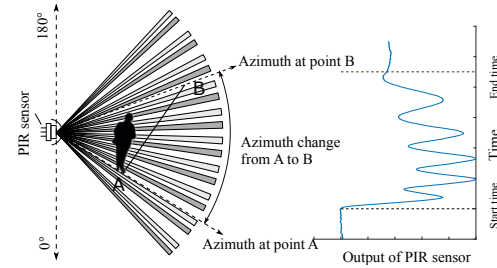


Figure 2: Basic idea of our approach: the azimuth change of a moving person can be estimated by counting the number of rising and falling edges of the output of a PIR sensor.

example, in some conditions, especially in the presence of noise, the azimuth change cannot be estimated accurately from the output of PIR sensors. By analyzing the physical property of PIR sensors, we find that using the PIR sensor's input inferred from the obtained output data can achieve much better performance. In addition, we find that when a person turns abruptly, the azimuth change cannot be estimated correctly. We propose two methods to address this challenge.

The contributions of this paper are as follows. Firstly, to the best of our knowledge, our work is the first to leverage the azimuth change of a moving person to build a PIR-based localization system. Secondly, we propose a set of methods to accurately estimate the azimuth change. These methods are based on the PIR sensor's physical model and do not require abundant labeled training data. Lastly, we build a practical PIR-based localization system which achieves a high localization accuracy.

2 RELATED WORKS

In this section, we give a brief survey about the existing device-free localization systems. We divide the existing works into two categories: non-PIR based and PIR based systems.

Non-PIR based device-free localization systems

Localization systems based on cameras may be the first and also the most widely deployed device-free localization systems [1, 20]. Besides using cameras, acoustic-based localization systems utilize dedicated microphone arrays or leverage a network of nodes to localize the source of sound of human [3, 21]. The localization system proposed in [22] utilizes electric field sensors to sense the changes in one's body electric potential. On the other hand, systems proposed in [2, 23] leverage densely deployed light sensors to detect one's location. More recently, RF-based device-free localization systems have received a lot of attention that utilize the RSS of wireless signals from a network of Zigbee nodes [4, 24], the FMCW radio from dedicated RF devices [25, 26], and COTS WiFi devices [6, 8–10, 27–29].

PIR-based device-free localization systems

Compared with existing systems such as those based on cameras, acoustic sensors and WiFi APs, the advantages of using PIR are multifold. When compared with camera-based systems, PIR sensors can work well in low-light environments and have less privacy concerns. When compared with Wi-Fi based systems, PIR sensors have lower cost and are generally much more energy efficient. In

addition, PIR sensors are immune to multi-path effect [12] and hence are intrinsically more robust in a changing environment.

Many PIR-based localization systems have been designed [13–18, 30–32]. Most of them take a PIR sensor as a ‘binary’ indicator. In addition, the works [13, 30, 31] introduced how to determine a single person’s real-time location while the works in [14, 15] introduced how to track multiple persons. Note that although the localization method proposed in [32] utilizes the positive and negative peaks in the raw output of PIR detectors, it still belongs to the traditional ‘binary-based’ approach, as the peaks are only utilized to determine the presence of a person in different detection zones. Recently, there are a few related works which utilize the raw output data of PIR sensors for localization [17, 18]. However, these systems are data-driven and require abundant training data to be collected. In addition, in the presence of different environments and different types of PIR sensors, the data usually need to be re-collected.

3 A PRELIMINARY DESIGN OF ESTIMATING THE AZIMUTH CHANGE

We first give a formal definition of the azimuth change. As shown in Fig. 3, the **azimuth change** corresponding to the traces $A - B$ w.r.t to the PIR sensor P , is defined as the included angle between the sides PA and PB , i.e. θ . To obtain θ , we rely on counting the number of fan-shaped zones shown in Fig. 3.

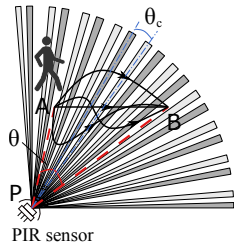


Figure 3: The definition of the azimuth change.

Fig. 4(a) shows the structure of a typical PIR sensor covered by Fresnel lens. The infrared radiation of a moving person (denoted as the dot) first goes through the Fresnel lens array, and then arrives at the sensing unit which consists of two parts, namely, a positive element and a negative one.

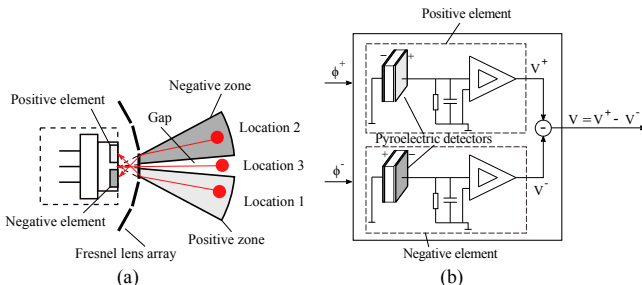


Figure 4: (a) The structure of PIR sensor and Fresnel lens, (b) simplified structure of the sensing unit of a PIR sensor.

Due to the above observation, when the heat source is at a certain location, say location 1 in Fig. 4(a), only the positive element will

receive the infrared radiation. Correspondingly, we say that location 1 is within a *positive zone* of the PIR sensor. On the other hand, when the heat source is at location 2, only the negative element receives its infrared radiation, and we say that location 2 is in a *negative zone* of the PIR sensor. Note that there exist other locations such as location 3, at which neither the positive nor negative element will receive the radiation. This indicates that there is a gap between the neighboring positive and negative zones.

Furthermore, the structure of Fresnel lens array [19] enables the following properties of the positive/negative zones: (1) Both positive and negative zones are approximately fan-shaped zones centered at the PIR sensor, and with similar center angles. (2) There are many fan-shaped positive and negative zones, and they are alternatively placed, with one zone adjacent by two opposite ones. (3) The angles of the gaps between adjacent zones are similar.

The above properties of fan-shaped zones can help us determine the azimuth change. More specifically, as shown in Fig. 3, let θ_c be the included angle between the symmetric axes of two adjacent fan-shaped zones. Then the azimuth change θ can be estimated by the equation as below:

$$\theta \approx N \cdot \theta_c \quad (1)$$

where N is the total number of fan-shaped zones covered by the trace $A-B$. Our next task is to find out N and θ_c .

To determine N

We first show how to determine N . As shown in Fig. 2, when a person moves in front of a PIR sensor, the PIR’s output oscillates like a sine wave, this enables us to obtain N by counting the number of rising and falling edges of the sine wave. The rationale of above statement can be attributed to the physical properties of PIR sensors. Fig. 4(b) shows the simplified internal structure of a PIR sensor’s sensing unit.

Let ϕ^+ and ϕ^- be the heat fluxes received by the positive and negative elements, respectively. The two elements respectively generate an output voltage, denoted as V^+ and V^- . The final output of the PIR sensor, denoted as V , is their difference: $V = V^+ - V^-$.

When a person is moving from a positive zone to a negative one, ϕ^+ keeps decreasing while ϕ^- keeps increasing. The above two effects combined to generate a decrease (i.e. a falling edge) in the PIR’s output. Similarly, when the person is walking from a negative to a positive zone, we can expect to see an increase (i.e. rising edge) in the PIR’s output.

As positive and negative zones of PIR sensors are alternatively placed to each other, an oscillating signal will be generated when a person is moving in front of a PIR sensor. Specifically, the total number of rising and falling edges is approximately equal to the number of zones one passes.

We utilize the following method to determine the number of rising and falling edges. First, we identify the peaks in the output signal of PIR sensors. Note that there are some peaks caused by environmental noise and should be eliminated. We utilize the feature called **prominence** [33], which measures how much a peak stands out due to its intrinsic height and its location relative to other peaks. A peak with small prominence is regarded as noise and will be eliminated. The threshold of prominence is determined by the statistics of peak prominence levels caused by noise and

by the human motion. Having determined the peaks, we can then calculate the number of rising and falling edges accordingly.

To determine θ_c

To estimate θ_c , we first locate the radii of all fan-shaped zones, then calculate all the included angles between the symmetric axes of adjacent zones. Then we take the average as θ_c . Unfortunately, the locations of the radii of fan-shaped zones are generally not available in the manual of PIR sensors. A typical manual only provides some optical parameters about the Fresnel lens array (e.g. the focal length, width and direction of each Fresnel lens) and the PIR sensor (e.g. the width of positive/negative sensing units and their distances).

We next explain how to leverage these parameters together with a simulation based approach to obtain θ_c . The idea is similar to the Monte Carlo method. We generate a point heat source in the sensing range of the PIR sensor. Then based on the optical parameters of the Fresnel lens array, we calculate where the infrared radiation of the heat source will be focused on after passing through the Fresnel lens array. If the radiation is located on the negative element, then we color the heat source as ‘dark’, indicating it is within a negative zone; if the radiation is focused on the positive element, the point heat source is colored as ‘gray’, indicating it is within a positive zone. Otherwise, the heat source will be made transparent. As an example, the point heat source 1 and 2 in Fig. 5 (a) are respectively colored as ‘dark’ and ‘gray’.

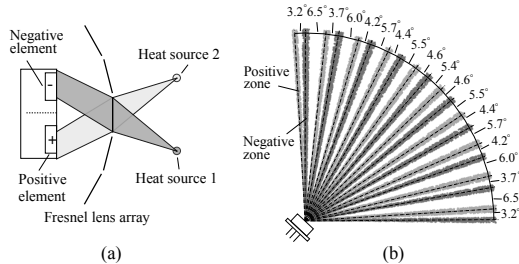


Figure 5: Using the simulation method to determine θ_c of a PIR sensor. (a) How to color a simulated heat source. (b) The obtained layout of the PIR sensor.

Then we generate a large number of point heat sources uniformly distributed within the sensing range of a PIR sensor. After all the points are colored, the boundaries of all the positive and negative zones emerge. The locations of the radii of all the positive and negative zones can be obtained by the boundaries of points with the same color. An example is shown in Fig. 5(b).

Having identified the locations of all radii, we then find out the symmetric axis for each zone. The included angles of the symmetric axes between two neighboring zones are averaged to obtain θ_c . Note that for three neighboring zones, like positive-negative-positive, the included angles of the first two and the last two are generally different. As shown in Fig. 5(b), the included angle between the symmetric axes of the top positive zone and of the lower negative zone is 3.2° , while the angle of the negative zone and lower positive one is 6.5° . The average of all neighboring included angles shown in Fig. 5(b), i.e. θ_c , is 4.9° . We find through experiments that the aforementioned simulation based approach can generate an accurate estimation of θ_c . The detailed validation experiments and the results will be introduced in Section 7.1.

4 ENHANCED DESIGN

In this section, we introduce two important enhancements that can significantly improve the performance of the system.

4.1 Enhancement 1: Utilizing input instead of output of PIR sensor

In the previous section, we demonstrate that N (the number of zones corresponding to the azimuth change) can be estimated by counting the number of rising and falling edges in the output data of PIR sensors. However, this approach may not give an accurate estimation of N , especially in the following two scenarios.

First, when a person moves relatively fast, being far away from a PIR sensor, or moves parallel to the zones of a PIR sensor, the amplitude of the PIR’s output is relatively small. Considering the effect of noise, it is not always easy to determine whether a rising or falling edge is caused by the person’s movement or by noise, which generates error in N . An example is shown in Fig. 6(a), where the output data of a PIR sensor are illustrated. The data are collected when a person is moving at about 2m/s and about 5 meters away from the PIR sensor. We can see that the PIR sensor’s output oscillates slightly, and its amplitude is comparable to that caused by noise when the person is static. As the experiment is carried out in an outside but controlled environment, we believe these oscillations are caused by the wind, since the amplitude of these oscillations increases with the speed of the wind. The wind slightly changes the temperature of the PIR sensor, and further affects the PIR sensor’s output signal. Due to these oscillations, it is difficult to obtain a proper threshold to distinguish a real rising/falling edge caused by movement and a pseudo one caused by noise, thus introducing error in N .

Second, we find that when a moving person stops, a PIR sensor generates some pseudo rising or falling edges. An example is shown in Fig. 6(b). These pseudo edges are caused by the dynamic characteristics of PIR sensors. When a person stops moving, although the sensor’s input becomes stable immediately, the output of the system will still oscillate for a while before it becomes stable, generating pseudo edges. These pseudo edges also contribute to the estimation errors.

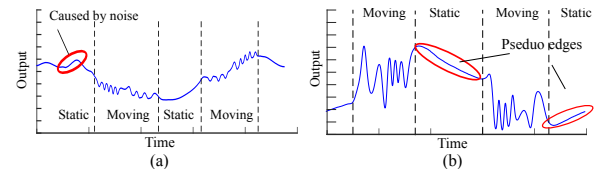


Figure 6: Two typical scenarios when N cannot be estimated accurately. (a) When a person moves fast, (b) when a moving person suddenly stops.

We next explain how to handle the above issues. We have shown in Fig. 4 the internal structure of a PIR sensor. Considering the symmetry of the positive and negative elements, the effect of two inputs (i.e. heat fluxes) of PIR sensor, ϕ^+ and ϕ^- , can be replaced by their difference, i.e. $\phi^d = \phi^+ - \phi^-$. Thus, the PIR sensor can be approximately represented as a dynamic system with input ϕ^d and output V .

The system’s input ϕ^d is the difference of the heat fluxes, and is abbreviated as **DHF**. The output of the system is the original PIR

sensor's output V . The system can be characterized as a second-order dynamic system as follows [34]:

$$G(s) = \frac{V(s)}{\phi^d(s)} = \frac{As}{Bs^2 + Cs + 1} \quad (2)$$

where the $G(s)$ is the transfer function of the PIR sensor; $V(s)$ and $\phi^d(s)$ are the Laplace transform of $V(t)$ and $\phi^d(t)$, respectively. The parameters A, B, C are determined by the internal electric circuits of the PIR sensor.

Generally speaking, the system described in Eq. 2 can be regarded as a low-pass filter. In other words, *the PIR sensor's output is essentially a filtered version of the DHF*. Furthermore, we can see from a broader perspective how a person's infrared radiation will affect the output of a PIR sensor. As shown in Fig. 7, when a person is moving in front of a PIR sensor, the person's infrared radiation will first pass through the Fresnel lens array to generate the DHF, which passes through the system of the PIR sensor, and finally generates the output.

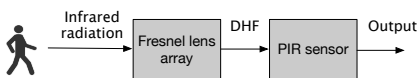


Figure 7: How a person's infrared radiation affects the output of a PIR sensor.

From a system point of view, the first unit in Fig. 7, i.e. Fresnel lens array, can be described as a linear system without delay. This is because ϕ^+ and ϕ^- at a certain time is directly determined by the area of the person's body in the corresponding zones at the same time [35]. Furthermore, when the person is in the center of a positive zone, the DHF will have a maximum value (i.e. a peak). Similarly, a person at the center of a negative zone will generate a minimum value (i.e. a trough). In contrast, the second unit in Fig. 7, i.e. PIR sensor, is a low-pass filter which inevitably introduces attenuation, smoothing and delay effect to the output.

The above discussion leads to a conclusion: **using DHF instead of the output of PIR sensors can potentially give a better estimation of N** , as the former is more directly affected by the infrared radiation than the latter.

For comparison, Fig. 8(a) shows the DHF collected from the experiment in which the output data have been shown in Fig. 6(a). We find that the rising and falling edges caused by the person's movement can be easily identified in DHF, which in turn gives a better estimation of N . In addition, Fig. 8(b) shows that there is no pseudo edges in the DHF.

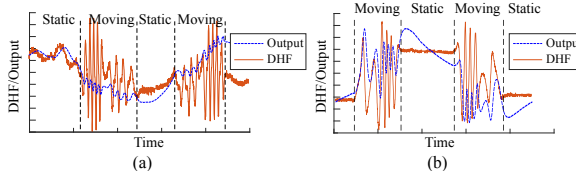


Figure 8: Using DHF to improve the accuracy of N .

In the rest of this section, we briefly introduce how to estimate the DHF. Given the output of a PIR sensor, to estimate its DHF in essence, is an inverse problem and can be solved by a technique called inverse filter [36].

Designing an inverse filter further requires the system parameters, i.e. the A, B and C in Eq. 2. To identify these three parameters, we design a simple experiment that generates a step input to the PIR sensor, and then measure the system's output, which is generally called as step response in control engineering. According to Eq. 2, the theoretical step response can be represented as a function of A, B, C . Then these three parameters can be estimated using some optimization method similar to curve fitting.

The experiment to generate the step input is as follows. First, we cover the PIR sensor with a box that can isolate outside infrared radiation. Then we set the temperature of a soldering iron about 250° and move it about 0.5 meter from the PIR sensor. Finally, we remove the box promptly to generate an abrupt constant input, i.e. a step, to the PIR sensor. We repeat the above experiment 10 times, and all the collected data are combined to estimate the corresponding parameters. Having identified the system parameters, we then utilize the inverse filtering technique to estimate the DHF from the output of PIR sensor.

The above procedures only need to be carried out once for a certain type of PIR sensors. Experiments have shown that for a localization system using multiple PIR sensors of the same type, using parameters obtained from a single PIR sensor can achieve almost the same performance as that when the parameters from each PIR sensor are determined respectively.

4.2 Enhancement 2: Handling abrupt turning

We have shown in Section 3 that even when a person is walking on a curved trace (as shown in Fig. 9(a)), the azimuth change can be estimated accurately by the product of the number of zones he crosses (i.e. N) and θ_c . In this example, the azimuth change corresponding to curves A-B is $\theta = 8 \cdot \theta_c$.

However, things will be different in Fig. 9(b). On the curve of A-B, the person crosses a total of 8 zones (four during A-C and four during C-B). Correspondingly, the azimuth change is $\theta = 8 \cdot \theta_c$. However, according to Fig. 9(b), the actual azimuth change of trace A-B is 0° .

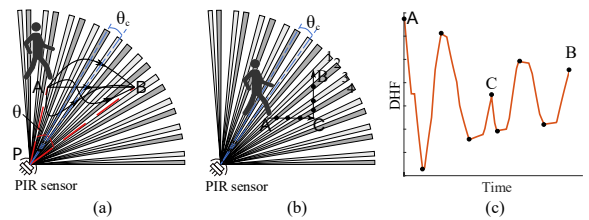


Figure 9: (a) Conditions when N can be estimated accurately. (b) The previous method fails if the trace contains abrupt turning points. (c) The DHF for the trace in (b).

The key difference between the traces shown in Fig. 9(a) and Fig. 9(b) lies in the change of direction during A-B. In the former, the person's walking direction remains to be clockwise from A-B. In contrast, the direction of the curve in the latter starts from clockwise (A-C) but then changes to anticlockwise (C-B) at point C. For convenience, we define points where the direction changes from clockwise to anticlockwise (or vice-versa) as the **turning points**. The presence of turning points makes the previous azimuth change estimation method fail.

To address this issue, we first detect these turning points and then estimate N s accordingly. Use the example shown in Fig. 9(b). If we know there is a turning point C on trace A-B, we can use the following equation to estimate the azimuth change θ during A-B:

$$\theta \approx |N_1 - N_2| \cdot \theta_c \quad (3)$$

where N_1 and N_2 are the number of the zones crossed before and after turning point C, respectively.

Eq. 3 can be generalized to conditions where a trace contains multiple turning points. In these conditions, M turning points will divide the whole trace into $M + 1$ sections, and these sections can be divided into two categories. Sections in the same category will have the same direction (clockwise or anti-clockwise). Then we simply let N_1 be the number of zones crossed in the first category and N_2 be the number of zones in the second category, and utilize Eq. 3 to obtain the azimuth change during the whole period.

We next explain how to identify the turning points. Fig. 9 (c) shows the DHF of a PIR sensor when a person moves along the trace shown in Fig. 9 (b), and there is a small local maximum C. This point exactly corresponds to the turning point C in Fig. 9(b) and the reason is as follows. When the person moving on the trace A-C is leaving the negative zone 4, the DHF starts to increase. However, he makes a turn at point C and then approaches to zone 4 again, and the DHF will then decrease and we can see a local maximum in the DHF. Likewise, if C is located in the middle of zone 3 and 4, the DHF will have a local minimum. To summarize, a turning point will generate a local extrema in DHF, and we can utilize this character to detect turning points.

However, as crossing positive or negative zones will also generate local extrema, we need to determine whether a local extremum is caused by abrupt turning or by crossing a zone. We propose a simple threshold method to identify turning points. In our method, a peak/trough is considered to be caused by turning if its absolute height is smaller than a certain percentage of the previous one. Based on our experiments, we find that a small threshold may miss identifying many turning points while a large threshold can lead to many falsely identified turning points. Fig. 10 shows the true positive rate (TPR) and the false positive rate (FPR) with the increase of the threshold. As the estimation period is generally set to be short (less than 1s), low FPR is more favorable, as the presence of turning points in a single period is not common. In addition, the consequence of missing identifying turning points can be further alleviated by using other information such as the motion model of a person. Based on this discussion, we set the threshold to be 0.5, which can achieve about 3% FPR, while the TPR is about 47%.

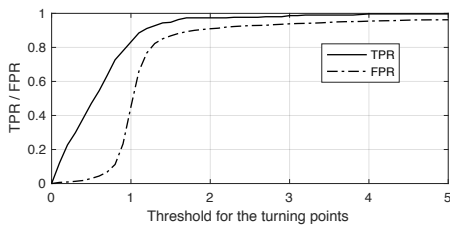


Figure 10: The TPR and FPR of identifying turning points with the change of threshold.

In addition, we notice that when an estimation period is short, the probability of having in that period is small. For example, instead

of estimating the azimuth change for the whole trace A-B in Fig. 9(b), we can adopt a shorter estimation period that divides A-B into two sections: A-C and C-B. In this case, the estimation accuracy can be improved.

However, the duration of the estimation period cannot be too short. If a person is walking as in Fig. 9(a), a longer estimation period normally gives a better estimation of θ . In addition, an estimation period should be long enough to contain at least one or more crossed zones to give a good estimate of N . Through experiments, we set the estimation period to 0.5s in our system, and the justification of choosing this value will be shown in Section 7.4.3.

4.3 Double windowing and fractional N

In this section, we give more details on the estimation of N . As N needs to be identified in real-time, a simple approach to identify N is to set a moving window. To achieve the real-timeliness, the length of the window is generally short. However, using the prominence to identify peaks of a short signal can suffer from the boundary-effect, where some spurious peaks can be identified at two ends of the window. In addition, in most conditions, we always have the extra parts of falling or rising edges besides the complete ones, which means that only estimating the number of complete falling and rising edges in a window can generate extra errors.

To alleviate the boundary-effect, we propose a double-windowing technique. As illustrated in Fig. 11, two moving windows, a long window, with length 2s, and a short one, within length 0.5s, are adopted, and the long window is 0.5s ahead of the short window. Instead of directly identifying N within the short window, we first identify peaks within the long window, and count those falling into the short window to obtain N .

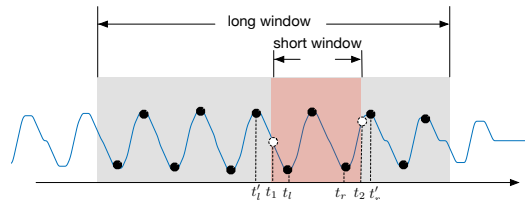


Figure 11: Using double windowing and fractional N .

To address the inaccuracies caused by the incomplete falling and rising edges, besides identifying the integer part of N (denoted as N_{int}), we also identify the fractional part of N . As shown in Fig. 11, we first identify the left point of the short window, which is t_1 . Then we identify the two end points of the edge containing t_1 , which is t'_l and t_l , correspondingly. The fractional part for the left side, denoted as N_l , is calculated as the ratio of the length of the edge which falls within the window and the length of the whole edge (i.e. $N_l = \frac{t_l - t_1}{t_l - t'_l}$). The fractional part for the right side, denoted as N_r , can be calculated in a similar manner (i.e. $N_r = \frac{t_2 - t_r}{t'_r - t_r}$ in this example). The final N is the summation of these three parts:

$$N = N_{int} + N_l + N_r \quad (4)$$

5 LOCALIZATION BY AZIMUTH CHANGE

In this section, we describe how to localize a moving person based on the information of azimuth change. We adopt a widely used localization algorithm called particle filter [37] in PIRATES. To use this algorithm, we first build a *system model*, which describes how the internal states (i.e. location, velocity, etc.) of a moving object change with time, and an *observation model* that describes the relationship between the above internal states and the observed information (i.e. the azimuth change). We utilize a classic system model below:

$$\begin{bmatrix} x_k \\ y_k \\ \dot{x}_k \\ \dot{y}_k \end{bmatrix} = \begin{bmatrix} 1 & 0 & T & 0 \\ 0 & 1 & 0 & T \\ 0 & 0 & 1 & 0 \\ 0 & 0 & 0 & 1 \end{bmatrix} \begin{bmatrix} x_{k-1} \\ y_{k-1} \\ \dot{x}_{k-1} \\ \dot{y}_{k-1} \end{bmatrix} + \mathbf{u}_k \quad (5)$$

where x_k and y_k are the x and y coordinates of a moving person at the k th observation time; \dot{x}_k and \dot{y}_k are the corresponding velocities; T is the estimation period; \mathbf{u}_k is the noise that characterizes the uncertainty in the system model.

To build the observation model, we first find the relationship between the states and the azimuth change. As shown in Fig. 12, assume the PIR sensor is located at (a, b) , the azimuth change at time k (i.e. θ_k) can be determined by the current state vector $[x_k, y_k, \dot{x}_k, \dot{y}_k]$ through the law of cosines:

$$\cos \theta_k = \frac{ap_k^2 + bp_k^2 - ab_k^2}{2ap_k \cdot bp_k} + n_k \quad (6)$$

where n_k is the observation noise; ap_k , bp_k and ab_k can be expressed by the state vector as below:

$$\begin{cases} ap_k = \sqrt{(x_k - T\dot{x}_k - a)^2 + (y_k - T\dot{y}_k - b)^2} \\ bp_k = \sqrt{(x_k - a)^2 + (y_k - b)^2} \\ ab_k = T \cdot \sqrt{\dot{x}_k^2 + \dot{y}_k^2} \end{cases}$$

Since Eq. 6 applies to all PIR sensors, this gives us a set of equations which forms the observation model. Having known the system model and the observation model, we utilize the particle filter framework [37] to determine the person's real-time location. The number of particles is set to be 10k, and the convergence rate is in the inverse of the number of particles [38]. As the particle filter updates locations iteratively, a single iteration takes about 20ms using our laptop computer with Intel's Core i7-6700 Processor.

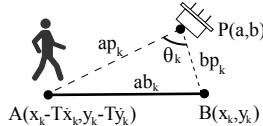


Figure 12: Relationship between azimuth change and moving states of a person.

6 MULTI-PERSON LOCALIZATION

In this section, we extend the proposed approach to multi-person scenarios. In the presence of multiple persons, the input signal of a PIR sensor, denoted as DHF, is approximately the superposition of

the input signals generated by individual persons:

$$DHF = \sum_{i=1}^M DHF_i + w \quad (7)$$

where DHF_i is the input signal on this PIR sensor when only the i^{th} person is present, and w is the noise. The major source of w comes from the blocking effect of human body, which occurs when the infrared radiation from a moving person is blocked by other persons in front of a PIR sensor. This is similar to the common Non-line-of-sight (NLOS) problem that many localization systems face [39].

We find through abundant simulations and experiments that the identified number of rising and falling edges in a DHF signal, denoted as N , is approximately the maximum N_i extracted from all the DHF_i signals, i.e.

$$N \approx \max\{N_1, \dots, N_M\} \quad (8)$$

where N_i is the number of rising and falling edges extracted from signal DHF_i .

The intuitions behind Eq. 8 are multi-folds. Firstly, in a small estimation period, DHF is often dominated by the DHF_i with the highest amplitude, which generally corresponds to a person closest to the PIR sensor. Furthermore, a person moving closer to a PIR sensor has a higher angular velocity on average, which generally corresponds to a DHF_i with large N_i . Secondly, the algorithm used to extract N_i , as described in Section 3, removes the low frequency content in DHF. It follows that the DHF_i with the largest N dominates the DHF, as shown in Eq. 8.

As an illustration, Fig. 13 shows a small section of simulation result in a two-person scenario. In this simulation, two persons are moving at a constant speed (1m/s) along two traces, with distances to the PIR sensor being 1.3m and 2.6m, respectively. We can see that as Person 1 is much closer to the PIR sensor than Person 2, DHF_1 has a much larger amplitude and higher frequency than DHF_2 . As a result, the number of rising and falling edges extracted from DHF_1 is 7, which is equal to that extracted from DHF_2 .

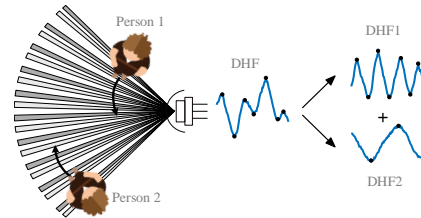


Figure 13: An example to illustrate Eq. 8.

Based on Eq. 8, we further have

$$N \cdot \theta_c \approx \max\{\theta^1, \dots, \theta^M\} \quad (9)$$

where θ^i is the azimuth change corresponding to the i^{th} person. Note that Eq. 9 establishes the relationship between sensor observations (N is extracted from the DHF signal) and the locations of multiple persons (θ^i is associated with the trace of the i^{th} person). Note that the above equation holds even when some persons are standing still, as their N_i s are nearly zero.

We carry out experiments to validate Eq. 8 and Eq. 9. In these experiments, we let two and three persons move randomly in the

sensing area of a PIR sensor (a circular sector with radius 9m and angle 90°) and we record the traces (to obtain θ^i) as well as the DHF signal (to obtain $N \cdot \theta_c$). Fig. 14 (a) shows the absolute error between $N \cdot \theta_c$ and the maximum azimuth change $\max\{\theta^1, \dots, \theta^M\}$. Fig. 14(b) illustrates the cumulative distribution function (CDF) of the errors. It can be seen that, in the 2-person scenario, about 80% errors are less than 4° . The error increases slightly in the 3-person scenario, due to more frequent blocking effects mentioned earlier.

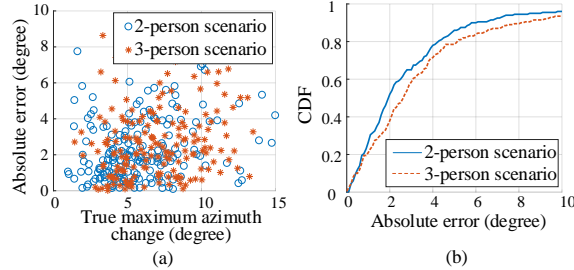


Figure 14: (a) The absolute error of Eq. 9 in 2-person and 3-person scenarios, (b) the CDF of the errors.

To determine the locations of multiple persons, we can establish a system model for each person as in Eq. 5. The observation model of each PIR sensor is described in Eq. 9. Note that we need to adapt it for each estimation period and combine the models of all deployed PIR sensors.

Finally, Eq. 9 assumes that the number of persons M is known a priori, which however, may not hold in practice. To estimate the value of M , we can deploy some devices at the entrances and the exits of the localization area [40, 41]. By counting the number of people entering and exiting the area, we can estimate the number of people in the area. An alternative approach is to take inputs from deployed PIR sensors and feed them into a pre-trained classifier like supporting vector machine (SVM) [42] to find out M . Some useful features that can be obtained from the DHF signal include the number of rising/falling edges, the kurtosis, and the entropy. We test the performance of the second approach and the experiment results show that the classification accuracies for 1-person, 2-person and 3-person scenarios can achieve 94%, 78% and 80%, respectively, using only 5-second data. When 30-second data are utilized, the accuracies can reach 97%, 91% and 92% respectively.

The experiments above show that the classification accuracy for 2-person scenarios is slightly lower than that of 3-person ones. Here, Fig. 15 shows the confusion matrix of the results using 5-second data. We can see that the slightly lower accuracy of 2-person scenarios is due to the higher possibility of wrongly classifying a 2-person scenario as a 1-target one (5%). In contrast, only 2% of 3-person scenarios are misclassified into 1-person scenario.

7 EXPERIMENTS

7.1 The PIR sensor and its sensing zones

We adopt PIR sensor Tranesen-PCD-2F21, and the Fresnel lens array YUYING-8719. They are off-the-shelf devices and widely used in many PIR applications. The detection range of each PIR sensor is about 10m, and the sampling frequency of each PIR sensor is set to be 60Hz. In addition, each PIR sensor has a communication module CC2530 to transfer the collected data to a host node, which consists

	1-person	2-person	3-person
True class	94%	5%	1%
2-person	5%	78%	17%
3-person	2%	18%	80%

1-person 2-person 3-person
Predicted class

Figure 15: Confusion matrix of people counting using 5s-data.

of a CC2530 and a CP2102 (a USB-to-UART Bridge Controller). The cost of a typical PIR-based system with 4 PIR sensors is about \$20, including 4 PIR sensors (\$4*0.7), the corresponding Fresnel lens arrays (\$4*0.5), the communication modules (\$4*3), and the host node (about \$4).

To estimate the azimuth change, we need to first find out θ_c . At the end of Section 3, we introduce a Monte Carlo-like method to estimate θ_c . The experimental setup is illustrated in Fig. 16. We place a bottle of hot water, as a heat source, 0.5m away from the PIR sensor. The PIR sensor, along with the Fresnel lens array, is put on a rotation plate which can rotate at a pre-defined constant speed. In our experiment, we set the rotation speed to $15^\circ/\text{s}$.

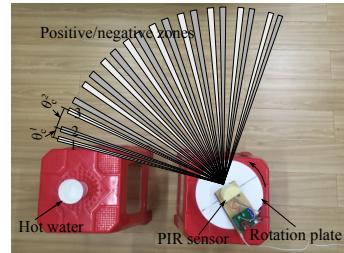


Figure 16: The experimental setup to identify the layout of positive/negative zones of the PIR sensor.

Fig. 17 shows a section of the DHF data obtained from the above experiment. We can see that the DHF has 10 peaks and 10 troughs, that corresponds well with the description of the manual that the PIR sensor has 20 zones (10 positive and 10 negative). A peak/trough in the DHF data indicates that the heat source is at the symmetric axis of a positive/negative zone. For example, points 1, 2, and 3 in Fig. 17 correspond to time instants when the bottle of hot water passes the symmetric axes 1, 2, and 3 shown in Fig. 16, respectively.

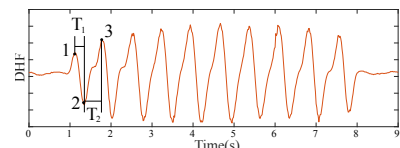


Figure 17: The DHF data and how the peaks/troughs correspond to the time instants in Fig. 16.

Correspondingly, based on the DHF data, we first identify all peaks and troughs, and then calculate the gaps between neighboring peaks and troughs. For example, T_1 shown in Fig. 17 measures the gap between the first peak and first trough, this corresponds to the θ_c^1 shown in Fig. 16 based on $\theta_c^1 = T_1 \cdot \omega$, where ω is the angular speed of the rotation plate. The equation above holds for all the

neighboring zones. Fig. 18 shows the obtained θ_c^i ($i = 1 \sim 19$) and the simulated θ_c^i introduced in Section 3. The absolute error of estimated θ_c^i has the mean 0.53° and the standard deviation 0.35° .

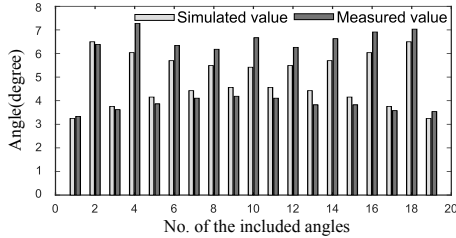


Figure 18: The obtained θ_c^i ($i = 1 \sim 19$) and the simulated θ_c^i .

Furthermore, we take the average of all θ_c^i and obtain the averaged value $\theta_c = 5.1^\circ$. This value is very close to 4.9° obtained from the simulation. This demonstrates that the proposed simulation approach can estimate the θ_c of PIR sensors accurately.

7.2 Estimation accuracy of azimuth change

In this section, we evaluate the estimation accuracy of the azimuth change. We design three types of scenarios shown in Fig. 19. In the first scenario (Fig. 19(a)), we let one person move along three arcs, $A_1 - B_1$, $A_2 - B_2$ and $A_3 - B_3$, all centered at the PIR sensor but with different radius. Our objective is to test the performance of the proposed azimuth change estimation method when a person is moving perpendicularly to the zones of a PIR sensor. In the second scenario shown in Fig. 19(b), the person is moving on traces approximately parallel to the zones. In the third scenario shown in Fig. 19(c), the person walks along $A - B$, and then makes turns to C_1, C_2 and C_3 , respectively. Our goal is to test the performance of the proposed method in the presence of abrupt turning points.

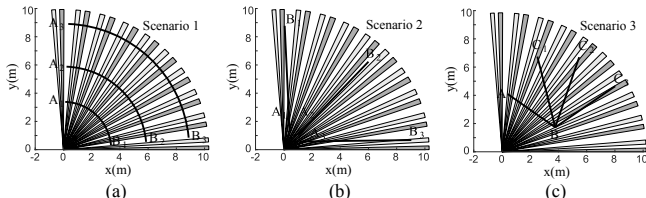


Figure 19: Three scenarios to test the accuracy of the azimuth change estimation.

The experimental setup is shown in Fig. 20. In particular, having obtained the layout of the zones of the PIR sensor, we ‘draw’ the layout on the floor using white strings shown in Fig. 20. These strings correspond to the edges of the estimated zones. The PIR sensor is aligned with the string-based layout. The purpose of establishing such a string-based layout is to guide the person to move along the predefined curves. We conduct 6 experiments in total at 3 different velocities ($0.8m/s$, $1.2m/s$ and $1.6m/s$), twice for each velocity. The deployment height of PIR sensors is about $1.5m$.

The CDFs of the estimation errors of the azimuth change in the three scenarios are shown in Fig. 21. In Fig. 21(a), we can see that the inner arc $A_1 - B_1$ (Trace 1) has the largest error while the outer arc $A_3 - B_3$ (Trace 3) has the smallest one. This can be attributed to the fact that the size of zones near the PIR sensor is much smaller than that of zones far away from the sensor. When a person is



Figure 20: Experimental setup.

very close to the PIR sensor, his body may occupy multiple zones simultaneously, and it is hard to identify peaks/troughs in DHF, leading to a larger estimation error.

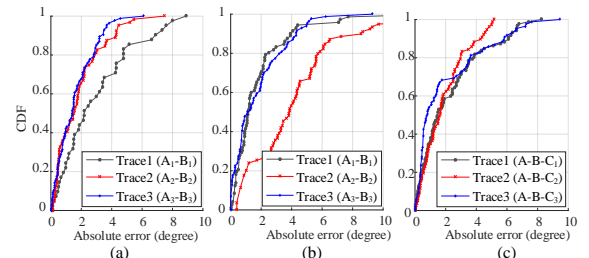


Figure 21: The CDFs of the error of the estimated azimuth change in the three scenarios shown in Fig. 19.

In Fig. 21(b), we observe that the estimation error on $A_2 - B_2$ (Trace 2) is much larger than the other two. By examining the traces in Fig. 19(b), we observe that Trace 2 is almost parallel to a zone of the PIR sensor, and the person does not cross a single zone. Correspondingly, the true azimuth change remains to be close to 0° . As DHF signals oscillate slightly in this case, it leads to a larger estimation error. The person on $A_1 - B_1$ (Trace 1) and $A_3 - B_3$ (Trace 3) does cross a few zones, and we observe smaller estimation errors. Fig. 21(c) shows that the presence of turning points did not affect the estimation error.

7.3 Localization accuracy of PIRATES

In this section, we demonstrate the performance of PIRATES in 6 different scenarios as shown in Fig. 22. The traces include simple straight lines (Fig. 22(a)) and more complex curves (Fig. 22(b)~Fig. 22(d)) in an area of $7m \times 7m$. In each scenario, we let the person walk along the pre-defined traces five times. In addition, we test the performance of the system when a person takes a random walk (Fig. 22(e)) and is walking in a $14m \times 14m$ area with more PIR sensor nodes deployed (Fig. 22(d)). The outputs of PIR sensor are transmitted to a host computer through wireless communication, and the DHF data are estimated to obtain the azimuth change. The estimated azimuth change is fed into the particle filter to obtain a real-time location. The ground-truth locations are collected through a UWB-based localization system YCHIOT-MINI3S, whose average localization error is about $10cm$.

Table 1 shows the statistics of the localization error in terms of mean and standard deviation. The detailed CDF of localization error is shown in Fig. 23.

We can see that PIRATES achieves sub-meter localization accuracy with 80% or higher probability in all scenarios. In particular,

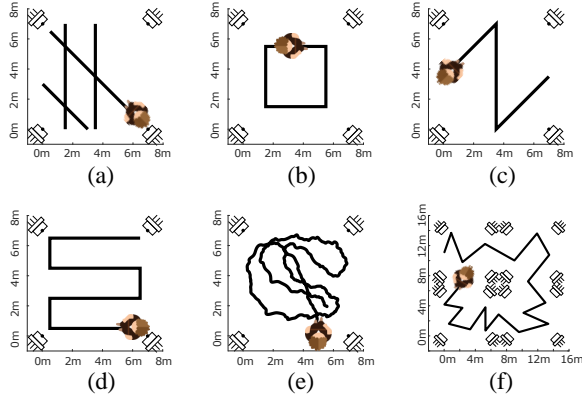


Figure 22: Six testing scenarios, (a) straight lines, (b) a square, (c) Z shape, (d) snake shape, (e) random walking, and (f) large area.

Scenario	Straight lines	Square	Z shape	Snake shape	Random walking	Large area
Mean (m)	0.47	0.69	0.66	0.71	0.67	0.66
Std (m)	0.41	0.37	0.41	0.45	0.50	0.46

Table 1: The statistics of error in 6 scenarios.

PIRATES achieves the best performance in scenario 1 (with sub-meter accuracy in 92%). The average localization error of all scenarios is about 0.64m with a standard deviation 0.48m. Even under the worst-case scenario, PIRATES can achieve localization error smaller than 1.9m with 99% probability. The results demonstrate the effectiveness of using the azimuth change for localization.

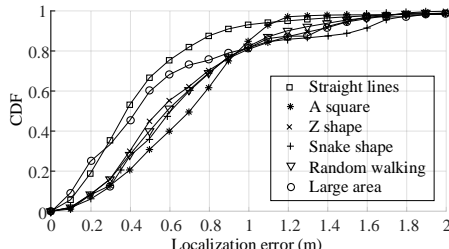


Figure 23: The CDFs of the localization error in 6 scenarios.

Comparing PIRATES with other PIR-based localization system [18]

We compare the localization performance of PIRATES with the one proposed in [18], which utilizes a data-driven approach to establish a model describing the relationship between the amplitude of PIR's outputs and its distance to a moving person. For a fair comparison, we use the same traces described in [18]. Please refer to Fig. 24 (a) and (b) as an illustration. In addition, [18] use ‘accuracy rate’, which is the probability of correctly localizing a person within a $1m \times 1m$ grid, to measure the performance, this is because they treat the localization problem as a classification task. We adopt the same performance metric in our experiment.

The results collected from the two scenarios are shown in Fig. 24(c). We can see that in both scenarios, PIRATES achieves better accuracy than the system described in [18]. In particular, the accuracy rate of our system is 0.54 and 0.78, which is 50% higher than that achieved by [18]. In addition, considering that the system proposed in [18] requires 8 PIR sensors and abundant training data,

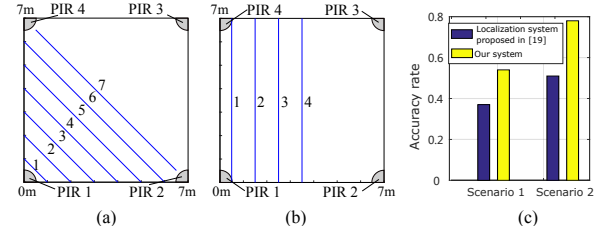


Figure 24: Experimental scenarios utilized in [18] and comparison result. (a) 7 slashed parallel traces, (b) 4 vertical parallel traces, (c) comparison results.

while our system only needs 4 PIR sensors and zero training data, the advantage of using azimuth change becomes apparent.

Multi-person localization accuracy of PIRATES

We test the performance of PIRATES in the presence of multiple persons. The first scenario is shown in Fig. 25(a), where two persons are moving side-by-side along a rectangle with constant speed about 1.2m/s. The distance between the two persons is about 1m. The corresponding distribution of localization error is shown in Fig. 25(c). In the second scenario shown in Fig. 25(b), the two persons are moving in the opposite direction along the rectangle, and the localization results are shown in Fig. 25(d).

We conduct two more experiments to test the performance of our system when multiple persons are walking randomly in the same indoor environment. Fig. 26(a) and Fig. 26(b) show the CDFs of localization errors in these two experiments. Note that in all the above experiments with multiple persons, we assume the number of persons can be estimated accurately (using the method proposed in Section 6). Table 2 summarizes the average localization error and the standard deviation of individual persons in these experiments.

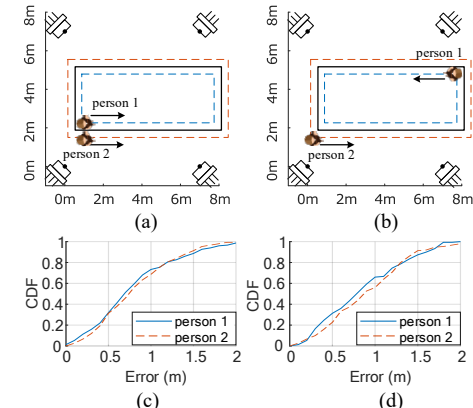


Figure 25: The multi-person scenarios when two persons are moving (a) side-by-side and (b) in the opposite direction along a rectangle. (c) (d) The CDFs of localization error of (a) and (b) respectively.

Scenario	#1	#2	#3	#4
Mean (m)	0.82 / 0.85	0.89 / 0.95	0.87 / 0.86	1.05 / 1.04 / 1.06
Std (m)	0.49 / 0.45	0.49 / 0.47	0.71 / 0.56	0.67 / 0.72 / 0.85

Table 2: The average localization error and standard deviation in the multi-person scenarios.

Compared to the single-person scenario, we observe that PIRATES has a lower accuracy in multi-person scenarios. In the presence of multiple persons, although theoretically we have $DHF \approx$

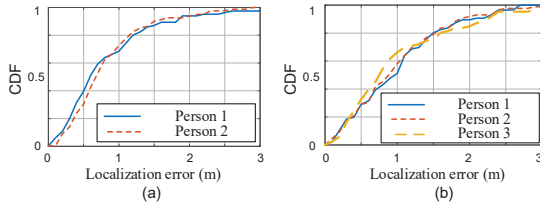


Figure 26: The CDFs of localization error of (a) 2-person and (b) 3-person scenarios, respectively.

$\sum_{i=1}^M DHF_i$ according to Eq. 7, it is not possible to reconstruct all the DHF_i using measured DHF signals. On the other hand, decoupling the effect of individual persons is based on N , the number of rising and falling edges in the DHF signal. However, the experimental results show that N is not the summation of individual N_i s, but approximately equals to the largest N_i (see Eq. 8). This makes it very difficult to recover each individual N_i , causing less accurate localization results.

We next discuss two possible ways to enhance the localization accuracy in the presence of multiple targets. One possible approach is to increase the number of deployed PIR sensors. We test our systems with 6 and 8 PIR sensors deployed on the area shown in Fig. 25(a) for the two-person scenario, and the average localization errors are 0.83m and 0.75m, respectively. Another approach is to leverage deep learning techniques to develop a data-driven localization system. We build a deep convolutional neural network to simultaneously estimate the number of people and their locations. The experimental results show that in the scenarios that involves at most 3 persons and 4 deployed PIR sensors, the average person counting accuracy is 95.6% using only 2.5-second data, and the average localization errors are respectively 0.43m, 0.65m, and 0.86m. However, these two approaches are not cost-free. Deploying more PIR nodes can increase the cost of the system. Using the data-driven approach requires abundant training data. For example, in the above experiment, 5-hour data for each of the 1,2 and 3 person-scenarios are required to train the network model.

7.4 More experiment results

In this section, we give more experimental results of PIRATES.

7.4.1 The effect of the deployments of PIR sensors. We first evaluate the impact of the number and the locations of PIR sensors on the localization accuracy. Fig. 27(a) shows four different types of deployments, denoted as ① ~ ④. Deployment ① refers to the scenario where only a single PIR sensor is deployed at the bottom left, while Deployment ② adds one more sensor at the bottom right. Deployment ③ further adds one more PIR sensor at the upper right, and Deployment ④ includes all 4 PIR sensors. Fig. 27(b) shows Deployment ⑤, where four PIR sensors are evenly spaced in a vertical line. Fig. 27(c) shows Deployment ⑥ and ⑦, in which 3 and 6 PIR sensors formed a triangle and a hexagon, respectively.

The CDFs of the localization error are shown in Fig. 28. The corresponding mean and standard deviation are shown in Table 3. We have the following observations. Generally speaking, the localization accuracy improves as the number of PIR sensors increases. Second, given the same number of PIR sensors, the localization accuracy is affected by the deployment of sensors. In particular, it is preferable to deploy sensors uniformly in an area. For example,

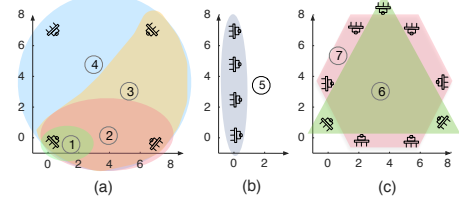


Figure 27: Different deployments of PIR sensors (a) Deployments ①~④, (b) Deployment ⑤, (c) Deployments ⑥ and ⑦.

Deployment ⑤, where 4 PIR sensor nodes are located on a vertical line, has a larger localization error than that of Deployment ④ in which the 4 sensors are located at four different corners.

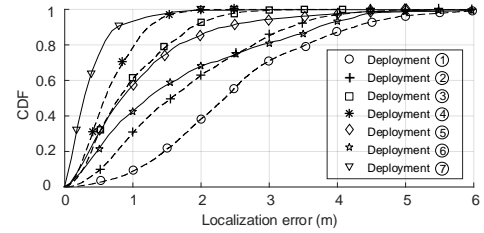


Figure 28: The CDFs of localization error in 6 deployments.

Scenario Error	1 PIR	2 PIR	3 PIR	4 PIR	line	triangle	hexagon
Mean (m)	2.42	1.66	0.92	0.67	0.98	1.23	0.32
Std (m)	1.26	1.17	0.68	0.50	0.71	0.98	0.27

Table 3: The localization error in different deployments.

7.4.2 Near-field scenario. In Fig. 21(a), we show that on the inner arc (Trace 1), the system has a greater estimation error about the azimuth change than on the outer arc (Trace 3). This may raise a concern that when a person is moving close to a PIR sensor, the localization error will increase significantly. However, we argue that a location close to a PIR sensor is generally far from other PIR sensors. This alleviates the negative effect of the low accuracy of azimuth change estimation for a close PIR sensor.

As an illustration, we analyze the results in the first 5 scenarios of Fig. 22. In particular, we divide the tracking area into two regions: the near-field region, in which the points are close to at least one PIR sensor, and the far-field region, in which the points are far from all the PIR sensors. We try different thresholds, ranging from 1m to 3.5m, to determine ‘near-field’ and ‘far-field’ regions.

Fig. 29 shows the difference between the average localization errors in near-field and far-field regions. We have three observations. Firstly, for all thresholds, the average localization error in near-field region is greater than that in the far-field one. Secondly, generally speaking, the difference of localization errors in the two regions decreases with the increase of the threshold. Thirdly, the overall differences on different thresholds are still relatively small, ranging from $0.02m \sim 0.1m$. This indicates that although moving nearby a PIR sensor could degrade the localization accuracy, this degradation is not significant.

7.4.3 The estimation period and the importance of turning point detection. At the end of Section 4.2, we mention that selecting an appropriate estimation period can alleviate the negative effect of

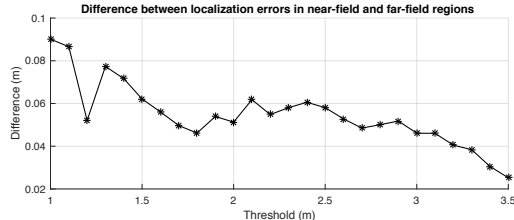


Figure 29: Difference of the errors in near-field and far-field regions.

missing identifying turning points. In this section, using data from the 6 scenarios in Fig. 21, we show the performance of the system at different estimation periods and how the turning point detection will affect localization accuracy.

The solid curve shown in Fig. 30 shows how the average localization error changes with different estimation period. We can clearly observe a ‘U’ turn when the estimation period changes from 0.1s to 2s. We observe that a very small estimation period like 0.1s will lead to a relatively large localization error, this is because in such a short period of time, the moving person is rarely able to cross a complete zone of the PIR sensor. On the other hand, a large estimation period like 2s may miss many abrupt turning points, which can have a negative effect on the localization accuracy. The localization error reaches its minimum at about 0.5s. In addition, the dashed curve shown in Fig. 30 illustrates the localization accuracy without using the turning point detection method described in Section 4.2. It can be seen that for all estimation periods, utilizing the turning point detection scheme can improve the localization accuracy.

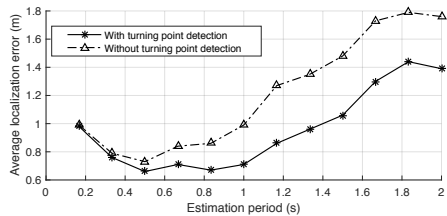


Figure 30: The effect of the estimation period and the turning point detection.

7.4.4 Theoretical insights on the effect of traces and sensor deployments on the localization accuracy. We next provide some theoretical insights on our observations from the previous section. Fig. 31(a) shows the scenario with only two PIR sensors, which are located at the top right and the bottom left respectively. Trace 1 and Trace 2 have the same length but are perpendicular to each other. We observe that the localization accuracy under Trace 1 is higher than that of Trace 2.

The rationale behind can be explained as follows. As Trace 1 is perpendicular to the line connecting the two PIR sensors, when a person is moving on Trace 1 from (x_1, y_1) to (x_2, y_2) , he will cross many zones that are covered by both PIR sensors. Therefore a slight movement on Trace 1 can lead to large variation in DHF, and generate a large azimuth change θ s on both PIR sensors, i.e., θ s are highly sensitive to the movement on Trace 1. As we rely on the azimuth change θ s to infer the location, this high sensitivity helps to decrease the localization error. In contrast, as Trace 2 is aligned with the fan-shaped zones of PIR sensors, a slight movement on Trace 2 will only generate small θ s. As a result, the localization

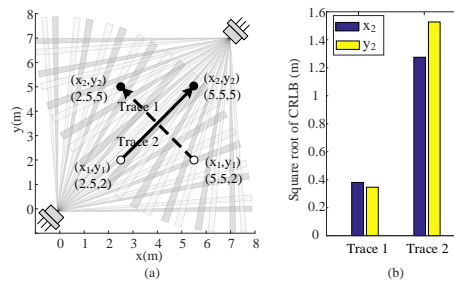


Figure 31: (a) An example of two traces. (b) The CRLB of the end coordinates of the two traces.

accuracy on Trace 2 is much lower than that on Trace 1. In summary, the localization accuracy is dependent on the sensitivity of the azimuth change to the change of locations. Fig. 31(a) shows that the sensitivity could be affected by the deployment of sensor nodes, the person’s current location, and the moving direction.

The above explanation can be characterized by the Cramer Rao Lower Bound (CRLB), which is widely used to evaluate localization accuracy [43]. To find out CRLB, we first build the joint probability density function about observed azimuth change and locations, and then calculate the Fisher information matrix (FIM) of the above function. The CRLB is the inverse of the FIM. We omit the theoretical details for brevity. Fig. 31(b) shows the CRLB of (x_2, y_2) for both traces. We can see that the CRLB on Trace 1 is much smaller than that on Trace 2, which is consistent with our observations.

8 DISCUSSIONS AND CONCLUSION

In this paper, we propose PIRATES, a PIR-based device-free localization system. From the raw output of PIR sensors, PIRATES extracts a type of information called as azimuth change, and utilizes the information to track the locations of one or more moving persons. PIRATES can achieve better accuracy than state-of-the-art PIR-based systems.

There are a few interesting directions to explore in the future. First, how to determine the optimal sensor deployment is an interesting and meaningful problem to be investigated. Second, as shown in Section 7.3, PIRATES has a low accuracy in the presence of multiple targets. The accuracy may further decrease with increasing number of targets. We have discussed the possibility of using a data-driven approach to enhance the localization accuracy, and the drawbacks of this approach are the large amount of data to be collected and the sensitivity to the change of environment. We believe a promising approach is to combine the physical model of PIR sensors (as in PIRATES) with the data-driven approach, such that the drawbacks of both approaches can be alleviated in the multi-person scenario.

ACKNOWLEDGMENTS

Xuefeng Liu is the contact author. This work was supported by National Natural Science Foundation of China (61976012, 61872410, 61772060), National Key R&D Program of China (2017YFB1301100), and CERNET Innovation Project (NGII20170315). We thank all the reviewers and our shepherd for their valuable comments and helpful suggestions.

REFERENCES

- [1] Tao Yang, Francine Chen, Don Kimber, and Jim Vaughan. Robust people detection and tracking in a multi-camera indoor visual surveillance system. In *2007 IEEE International Conference on Multimedia and Expo*, pages 675–678. IEEE, 2007.
- [2] Xufei Mao, Shaojie Tang, Xiaohua Xu, Xiang-Yang Li, and Huadong Ma. iLight: Indoor device-free passive tracking using wireless sensor networks. In *2011 Proceedings IEEE INFOCOM*, pages 281–285. IEEE, 2011.
- [3] Yukang Guo and Mike Hazas. Localising speech, footsteps and other sounds using resource-constrained devices. In *Proceedings of the 10th ACM/IEEE International Conference on Information Processing in Sensor Networks*, pages 330–341. IEEE, 2011.
- [4] Peter Hillyard and Neal Patwari. Never use labels: Signal strength-based bayesian device-free localization in changing environments. *IEEE Transactions on Mobile Computing*, 2019.
- [5] Ju Wang, Jie Xiong, Hongbo Jiang, Xiaojiang Chen, and Dingyi Fang. D-watch: Embracing “bad” multipaths for device-free localization with cots rfid devices. *IEEE/ACM Transactions on Networking*, 25(6):3559–3572, 2017.
- [6] Chitrar R Karanam, Belal Korany, and Yasamin Mostofi. Magnitude-based angle-of-arrival estimation, localization, and target tracking. In *2018 17th ACM/IEEE International Conference on Information Processing in Sensor Networks (IPSN)*, pages 254–265. IEEE, 2018.
- [7] Ju Wang, Hongbo Jiang, Jie Xiong, Kyle Jamieson, Xiaojiang Chen, Dingyi Fang, and Binbin Xie. Lifs: low human-effort, device-free localization with fine-grained subcarrier information. In *Proceedings of the 22nd Annual International Conference on Mobile Computing and Networking*, pages 243–256, 2016.
- [8] Xiang Li, Shengjie Li, Daqing Zhang, Jie Xiong, Yasha Wang, and Hong Mei. Dynamic-music: accurate device-free indoor localization. In *Proceedings of the 2016 ACM International Joint Conference on Pervasive and Ubiquitous Computing*, pages 196–207, 2016.
- [9] Kun Qian, Chenshu Wu, Yi Zhang, Guidong Zhang, Zheng Yang, and Yunhai Liu. Widar2. 0: Passive human tracking with a single wi-fi link. In *Proceedings of the 16th Annual International Conference on Mobile Systems, Applications, and Services*, pages 350–361, 2018.
- [10] Yaxiong Xie, Jie Xiong, Mo Li, and Kyle Jamieson. md-track: Leveraging multi-dimensionality in passive indoor wi-fi tracking. *arXiv preprint arXiv:1812.03103*, 2018.
- [11] Sidney B Lang. Pyroelectricity: from ancient curiosity to modern imaging tool. *Physics today*, 58(8):31, 2005.
- [12] Joseph M Kahn and John R Barry. Wireless infrared communications. *Proceedings of the IEEE*, 85(2):265–298, 1997.
- [13] Qi Hao, David J Brady, Bob D Guenther, John B Burchett, Mohan Shankar, and Steve Feller. Human tracking with wireless distributed pyroelectric sensors. *IEEE Sensors Journal*, 6(6):1683–1696, 2006.
- [14] Qi Hao, Fei Hu, and Jiang Lu. Distributed multiple human tracking with wireless binary pyroelectric infrared (pir) sensor networks. In *SENSORS, 2010 IEEE*, pages 946–950. IEEE, 2010.
- [15] Jaspreet Singh, Rajesh Kumar, Upamanyu Madhow, Subhash Suri, and Richard Cagley. Multiple-target tracking with binary proximity sensors. *ACM Transactions on Sensor Networks (TOSN)*, 8(1):1–26, 2011.
- [16] Iuliia Vlasenko, Ioannis Nikolaidis, and Eleni Stroulia. The smart-condo: Optimizing sensor placement for indoor localization. *IEEE Transactions on Systems, Man, and Cybernetics: Systems*, 45(3):436–453, 2014.
- [17] Gianluca Monaci and Ashish Pandharipande. Indoor user zoning and tracking in passive infrared sensing systems. In *2012 Proceedings of the 20th European Signal Processing Conference (EUSIPCO)*, pages 1089–1093. IEEE, 2012.
- [18] Sujay Narayana, R Venkatesha Prasad, Vijay S Rao, Tammo V Prabhakar, Sripad S Kowshik, and Madhuri Sheethala Iyer. Pir sensors: Characterization and novel localization technique. In *Proceedings of the 14th international conference on information processing in sensor networks*, pages 142–153, 2015.
- [19] Giuseppe A Cirino, Robson Barcellos, Luiz G Neto, Ronaldo D Mansano, Allan Bereczki, and Spero P Morato. Fresnel lens array with spatial filtering for passive infrared motion sensor applications. *Annals of Optics of the XXIX ENFM*, 2006.
- [20] John Krumm, Steve Harris, Brian Meyers, Barry Brumitt, Michael Hale, and Steve Shafer. Multi-camera multi-person tracking for easyliving. In *Proceedings Third IEEE International Workshop on Visual Surveillance*, pages 3–10. IEEE, 2000.
- [21] Michael S Brandstein and Harvey F Silverman. A practical methodology for speech source localization with microphone arrays. *Computer Speech & Language*, 11(2):91–126, 1997.
- [22] Tobias Grosse-Puppendahl, Xavier Dellangnol, Christian Hatzfeld, Biying Fu, Mario Kupnik, Arjan Kuijper, Matthias R Hastall, James Scott, and Marco Gruteser. Platypus: Indoor localization and identification through sensing of electric potential changes in human bodies. In *Proceedings of the 14th Annual International Conference on Mobile Systems, Applications, and Services*, pages 17–30, 2016.
- [23] Shuai Zhang, Kaihua Liu, Yongtao Ma, Xiangdong Huang, Xiaolin Gong, and Yunlei Zhang. An accurate geometrical multi-target device-free localization method using light sensors. *IEEE Sensors Journal*, 18(18):7619–7632, 2018.
- [24] Joey Wilson and Neal Patwari. Radio tomographic imaging with wireless networks. *IEEE Transactions on Mobile Computing*, 9(5):621–632, 2010.
- [25] Fadel Adib, Zach Kabelac, Dina Katabi, and Robert C Miller. 3d tracking via body radio reflections. In *11th {USENIX} Symposium on Networked Systems Design and Implementation ({NSDI} 14)*, pages 317–329, 2014.
- [26] Mingmin Zhao, Yonglong Tian, Hang Zhao, Mohammad Abu Alsheikh, Tianhong Li, Rumen Hristov, Zachary Kabelac, Dina Katabi, and Antonio Torralba. Rf-based 3d skeletons. In *Proceedings of the 2018 Conference of the ACM Special Interest Group on Data Communication*, pages 267–281, 2018.
- [27] Heba Aly and Moustafa Youssef. New insights into wifi-based device-free localization. In *Proceedings of the 2013 ACM conference on Pervasive and ubiquitous computing adjunct publication*, pages 541–548, 2013.
- [28] Souvik Sen, Jeongkeun Lee, Kyu-Han Kim, and Paul Congdon. Avoiding multipath to revive inbuilding wifi localization. In *Proceeding of the 11th annual international conference on Mobile systems, applications, and services*, pages 249–262, 2013.
- [29] Jon Gjengset, Jie Xiong, Graeme McPhillips, and Kyle Jamieson. Phaser: Enabling phased array signal processing on commodity wifi access points. In *Proceedings of the 20th annual international conference on Mobile computing and networking*, pages 153–164, 2014.
- [30] Suk Lee, Kyoung Nam Ha, and Kyung Chang Lee. A pyroelectric infrared sensor-based indoor location-aware system for the smart home. *IEEE Transactions on Consumer Electronics*, 52(4):1311–1317, 2006.
- [31] Xiaomu Luo, Baihua Shen, Xuemei Guo, Guocai Luo, and Guoli Wang. Human tracking using ceiling pyroelectric infrared sensors. In *2009 IEEE International Conference on Control and Automation*, pages 1716–1721. IEEE, 2009.
- [32] Jiang Lu, Ting Zhang, Fei Hu, and Qi Hao. Preprocessing design in pyroelectric infrared sensor-based human-tracking system: On sensor selection and calibration. *IEEE Transactions on Systems, Man, and Cybernetics: Systems*, 47(2):263–275, 2016.
- [33] The definition of peak prominence. <https://ww2.mathworks.cn/help/signal/ref/findpeaks.html>.
- [34] Andrzej Odon. Modelling and simulation of the pyroelectric detector using matlab/simulink. *Measurement Science Review*, 10(6):195–199, 2010.
- [35] Sami Aldalahmeh, Amer Hamdan, Mounir Ghogho, and Des McLernon. Enhanced-range intrusion detection using pyroelectric infrared sensors. In *2016 Sensor Signal Processing for Defence (SSPD)*, pages 1–5. IEEE, 2016.
- [36] Masato Miyoshi and Yutaka Kaneda. Inverse filtering of room acoustics. *IEEE Transactions on acoustics, speech, and signal processing*, 36(2):145–152, 1988.
- [37] Olivier Cappé, Simon J Godsill, and Eric Moulines. An overview of existing methods and recent advances in sequential monte carlo. *Proceedings of the IEEE*, 95(5):899–924, 2007.
- [38] Dan Crisan and Arnaud Doucet. A survey of convergence results on particle filtering methods for practitioners. *IEEE Transactions on signal processing*, 50(3):736–746, 2002.
- [39] Stefano Marano, Wesley M Gifford, Henk Wymeersch, and Moe Z Win. Nlos identification and mitigation for localization based on uwb experimental data. *IEEE Journal on selected areas in communications*, 28(7):1026–1035, 2010.
- [40] Florian Wahl, Marija Milenkovic, and Oliver Amft. A distributed pir-based approach for estimating people count in office environments. In *2012 IEEE 15th International Conference on Computational Science and Engineering*, pages 640–647. IEEE, 2012.
- [41] Huazhong Xu, Pei Lv, and Lei Meng. A people counting system based on head-shoulder detection and tracking in surveillance video. In *2010 International Conference On Computer Design and Applications*, volume 1, pages V1–394. IEEE, 2010.
- [42] Erin L Allwein, Robert E Schapire, and Yoram Singer. Reducing multiclass to binary: A unifying approach for margin classifiers. *Journal of machine learning research*, 1(Dec):113–141, 2000.
- [43] Linqing Gui, Mengxia Yang, Hai Yu, Jun Li, Feng Shu, and Fu Xiao. A cramer-rao lower bound of csi-based indoor localization. *IEEE Transactions on Vehicular Technology*, 67(3):2814–2818, 2017.